Physical and Mechanical Evolution of Ternary Geopolymer Mortars Under Various Curing Methods

Bolat Balapanov
Department of Architecture and Construction, Institute of Engineering and Technology, Korkyt Ata Kyzylorda University, Aitekebi 29A, Kyzylorda, Kazakhstan
balapanov.sci@gmail.com

Sarsenbek Montayev
Industrial Technological Institute, Zhangir Khan West Kazakhstan Agrarian and Technical University, 51 Zhangir Khan Street, Uralsk, Kazakhstan
montaevs@mail.ru

Orhan Canpolat
Department of Civil Engineering, Faculty of Civil Engineering, Yildiz Technical University, Istanbul 34220, Turkiye
canpolat@yildiz.edu.tr

Beyza Fahriye Aygun
Department of Civil Engineering, Istanbul University-Cerrahpasa, 34320 Avcilar, Istanbul, Turkiye
beyza.aygun@ogr.iuc.edu.tr (corresponding author)

Youssef Alkhabaze
Department of Civil Engineering, Faculty of Civil Engineering, Yildiz Technical University, Istanbul 34220, Turkiye
youssef.alkhabaze@std.yildiz.edu.tr

Mucteba Uysal
Department of Civil Engineering, Faculty of Civil Engineering, Yildiz Technical University, Istanbul 34220, Turkiye
mucteba@yildiz.edu.tr

Received: 25 June 2025 | Revised: 16 July 2025 | Accepted: 27 July 2025

 DOI: https://doi.org/10.48084/etasr.12938

ABSTRACT

This study explores the mechanical and microstructural performance of Geopolymer Mortars (GMs) formulated with 50% ground granulated blast furnace Slag (S) from Türkiye and 25% of either Fly Ash (FA), Diatomite (D), or Opacifier Waste (OP) from Kazakhstan, aiming to enhance the material sustainability through ternary alkali-activated systems. All precursors were sieved below 90 µm and activated using a 2:1 blend of 12M sodium hydroxide (NaOH) and sodium silicate (Na_2SiO_3) with an Activator-to-Binder (*A*/*B*) ratio of 0.7 silica modulus (*SM* = 3.29), producing a water-to-binder ratio of approximately 0.28. GMs were cured under ambient, thermal (80 °C/24h), and electrothermal regimes (30 V, 40 V, 50 V) for 1–24 h. The highest compressive strength (35.03 MPa) was achieved under thermal curing, while 40 V electro-curing reached 31.34 MPa at 4 h, equivalent to 89% of the thermal maximum in only 14% of the time. The flexural strength under 40 V peaked at 5.66 MPa, surpassing the thermal values (5.44 MPa), and delivered the highest flexural strength-compressive strength ratio (approximately 0.20), indicating improved ductility. The water absorption and apparent porosity dropped by 29.2% and 7.2%

under 40 V curing, while the bulk density increased to 2.04 g/cm³. The fuzzy logic and Multi-Criteria Decision Making (MCDM) analyses ranked the 40 V condition as the highest overall due to its efficient balance of strength, durability, and energy performance. These findings position the controlled 40 V electro-curing as a rapid, energy-conscious alternative to conventional thermal methods, particularly valuable for prefabricated applications and resource-constrained construction environments.

Keywords-geopolymer; diatomite; opacifier waste; electrical curing; physical and mechanical properties

I. INTRODUCTION

In Türkiye's material landscape, waste is a byproduct of production cycles, geochemical complexity, and technological change. Türkiye has a rich but often overlooked supply of industrial aluminosilicate materials. These include FA from lignite power plants in Afsin-Elbistan, Soma, and Cayırhan; blast furnace S from the metallurgical centers of Karabuk, Eregli, and Iskenderun; Miocene D deposits in Central and Eastern Anatolia; and ceramic residues from industries in Eskisehir, Bilecik, and Usak. Once considered low-value byproducts or pollutants, these materials are now increasingly seen as mineral resources with a chemical potential to be used into next-generation binder assemblages.

An approach that creates value through the chemistry of transformation itself is required, moving beyond the traditional cementitious methods that rely on energy-intensive calcination and CO_2-heavy processes with centralized supply chains. This means moving toward alkali-activated materials and GMs, which turn the industrial byproducts into construction materials that are functionally superior, environmentally adaptive, and optimized for regional use, distinct from the hydration-dependent model of Portland Cement (PC), which produces Calcium-Silicate-Hydrate (C–S–H) gels by a fixed thermodynamic process.

GMs are formedform through the dissolution of amorphous aluminosilicate phases in an alkaline solution, leading to the generation of cross-linked networks dominated by sodium or calcium aluminosilicate hydrate phases (N–A–S–H and C–A–S–H). Their structure, function, and durability vary according to the local material chemistries and environmental demands [1-3]. In Türkiye, FA is usually sourced from the higher-silica lignites with the higher Si/Al ratios, providing depolymerizable glassy phases, while blast furnace S contributes Ca^{2+} and Mg^{2+} ions. These ions promote the hardening through alkaline catalysis, increase the cohesion of the resulting gels, and enhance the matrix densification through calcium-assisted polycondensation. However, Türkiye's geopolymer trajectory diverges in blending the non-canonical mineral resources [4-13].

D—an amorphous, biogenic silicate of fossilized diatom shells found in basin-rich provinces, such as Tokat, Aksaray, and Kırsehir—adds not only additional reactive silica, but also serves a thermal and rheological function: enhancing the internal curing by storing and slowly releasing moisture, mitigating the shrinkage gradients, and facilitating a more uniform gel network formation. Its high internal surface area and pozzolanic properties allow it to act as a secondary activator, prolonging reactivity and stabilizing the matrix in ambient and thermally fluctuating curing conditions. Conversely, ceramic OP), often discarded due to its chemical inertness in alkali solutions, performs a critical role in microstructural engineering. These particles—composed primarily of thermally stabilized zirconia, titania, or feldspathic phases—act as fine fillers that improve the particle packing, control the pore geometry, and resist the thermal distortion. They do not dissolve, but densify, helping to bridge the microcracks, resist shrinkage, and improve the mechanical integrity over cyclic freeze–thaw or thermal exposure [14-18]. When blended with FA–S–D systems, such inert additives enable the construction of multifunctional matrices in which the chemical reactivity, physical stability, and durability are integrated across scales. However, the chemical optimization of the binder alone is not sufficient, particularly in Türkiye's diverse climatic, where ambient curing can be slow, unreliable, or nonviable, and where thermal curing—involving ovens, steam chambers, or sealed autoclaves—remains both infrastructure-intensive and environmentally challenging.

Electrical or Electrothermal Curing (EC) has emerged as a transformative innovation: a method by which electrical current (typically 30–50 V) is passed through embedded conductors or directly into the matrix, generating resistive heat through ionic conduction that initiates and sustains the geopolymer reactions from within. Unlike external heating, which relies on spatial diffusion and often results in thermal gradients, EC ensures that the thermal activation coincides with the reaction front, delivering energy precisely, where dissolution, diffusion, and gelation occur. This internal heating allows for a programmable, uniform, and energy-efficient curing condition, which is particularly well-suited to field-scale or rural construction contexts, where the infrastructure for high-temperature curing may be unavailable or costly. The thermoelectric environment created within the matrix accelerates the geopolymerization and modulates it, allowing for reaction–energy synchrony that reduces shrinkage, mitigates microcracking, and preserves the dimensional integrity.

Moreover, EC aligns with Türkiye's broader energy transition goals, as it permits binder activation using electrical sources that may be renewable, off-grid, or digitally controlled, allowing for smart manufacturing in both centralized and distributed contexts. This curing method also enables real-time tuning, in which voltage, conductivity, moisture retention, matrix evolution, and curing-time can be controlled. Within such an integrated system, the geopolymer binders shift from inert chemical products to reactive electromechanical systems, capable of regulating their transformation through feedback-responsive thermal dynamics. This paradigm redefines curing not as a passive phase but as an active co-constitutive process in which energy and matter evolve simultaneously. The industrial by-products, when curated, recombined, and electrothermally activated, represent not just a substitute for

cement, but a material in which the performance is inscribed rather than inherited.

The aim of this study is to revalorize Türkiye's underused mineral residues and transform them into regionally optimized, self-regulating, and advanced binder systems, using electrothermal methods that combine chemistry, conductivity, and climate adaptation.

This study examines the internal heat generation, reaction rates, and matrix evolution in locally sourced materials by applying low-voltage electrical curing (30 V, 40 V, 50 V) over different time scales (1 to 24 h), alongside conventional thermal curing at 80 °C. This laboratory work is complemented by the incorporation of ternary mixes comprising both chemically active (S, FA, D) and structurally inert (OP) materials to facilitate a broader access to the combined morphology-dependent curing energy governing the mechanical strength, porosity response, and thermal response. The novelty of this work lies in achieving energy-efficient activation while providing full-range property characterization—compressive strength, bending strength, density, and absorption—complemented by the microstructural analysis using Scanning Electron Microscopy (SEM) and X-Ray Diffraction (XRD). With this approach, traditional curing practices for GMs in cold or infrastructure-limited locations are redesigned, while the local mineral resources and climatic conditions provide an efficient, scalable alternative to conventional binder materials in Türkiye.

II. MATERIALS AND METHODS

A. Materials

The binder constituents employed in the present work were a multi-sourced and compositionally optimized mix of ground granulated blast furnace S, Class F FA, D, and OP of which the S and FA were sourced from Türkiye. In contrast, the rest of the constituents—D and OP—were collected locally from Kazakhstan. Each precursor material was dry ground and sieved to achieve a maximal particle size of less than 90 µm to ensure a homogenous distribution, right contact surface, and stable reactivity in the geopolymer system. S, having a 2.91 g/cm³ specific gravity and a 1150 kg/m³ bulk density, mainly comprises CaO (35.5%), SiO_2 (40.5%), and Al_2O_3 (12.8%), along with minor constituents of MgO and SO_3.

These constituents were validated by the application of X-ray Fluorescence (XRF) analysis and reflected a chemistry highly suited to alkali-activation processes, which enabled it to deliver high early-age reactivity, dense gelling, and fast setting through the dissolution of calcium ions in the aluminosilicate matrix. FA, sourced from the Catalagzi Thermal Power Plant, had a specific gravity of 2.3 g/cm³ and a bulk density of approximately 1010 kg/m³. The FA showed the typical sphericity of low-calcium ashes and had a high glassy phase content, which caused slow but sustained geopolymeric activity. Its principal constituents were identified to be SiO_2 (58.75%), Al_2O_3 (25.24%), and Fe_2O_3 (5.76%), which collectively provided a cumulative pozzolanic oxide content of almost 90% (SiO_2 + Al_2O_3 + Fe_2O_3 = 89.75%), much higher than the 70% level typically associated with good pozzolanic performance. This elevated cumulative glassy oxide content made the FA highly compatible for increasing the long-term strength, lowering heat development, and controlling shrinkage.

In contrast, D sourced locally from Kazakhstan had a very different role. It has a very low, 1.82 g/cm³-specific gravity, a 600 kg/m³ bulk density, and a structural internal micro-pore system coupled with very good humidity-buffering capacity and a huge surface area. These features induced higher free water absorption, internal humidity stabilization during the curing, and refinement of the hardened matrix's capillary system. Even though its direct reactivity was moderate, the predominantly siliceous (>79% SiO_2) composition assumed a synergistic function of matrix densification and pozzolanic balance. Simultaneously, the OP, from Kazakhstan, was employed primarily for volume filling. With a bulk density of approximately 950 kg/m³ and 2.51 g/cm³ of specific gravity, the grains of OP possessed intermediate granulometry and limited chemical reactivity. Yet, they provided improved packing density, lower interstitial void content, and a carrier of reacting phases, facilitating a more mechanically locked and dimensionally stable binder.

RILEM sand, with a fineness modulus of 2.20, bulk density of 1.53 g/cm³, a specific gravity of 2.65 g/cm³, and a maximum gradation of 2.0 mm, was used in accordance with ASTM C33 standards. The sand was of well-graded type distributed in the range of 0.15–2.00 mm and served as an inert aggregate to achieve granulometric uniformity and stable mechanical properties for the geopolymer matrix. Thus, the binder design in general, optimally balanced the early-age reactivity (through the application of S), latent strength development (through FA), internal curing and pore refinement (through D) [19-21], and supplementary mechanical strength (through OP), emulating a hybrid approach optimized for performance in both hot and cold climate zones on limited curing facilities. The chemical composition of S, FA, and D is presented in Table I.

TABLE I. CHEMICAL COMPOSITION OF S, FA, OP, AND D BASED ON PRIMARY OXIDE CONTENTS

Material	MgO (%)	Al_2O_3 (%)	SiO_2 (%)	P_2O_5 (%)	SO_3 (%)	Cl (%)	K_2O (%)	CaO (%)	TiO_2 (%)	Fe_2O_3 (%)	MnO (%)
S	5.80	12.80	40.50	-	0.18	-	-	35.50	0.75	1.10	-
FA	2.22	25.24	58.75	0.84	-	-	-	1.46	-	5.76	-
OP	0.55	4.26	82.89	0.44	-	-	2.62	1.34	0.76	6.77	-
D	0.72	5.43	79.70	0.41	-	2.11	2.18	1.13	1.03	6.72	-

B. Mix Design

To investigate the interaction of aluminosilicate and CaO-rich precursors within GMs, a standardized set of mortar recipes was prepared using combinations of S, Class F-FA, D, and OP. For a comparative study of individual binder elements in geopolymerization processes, the focus was on their

contributions to reactivity, matrix structure evolution, and mechanical behavior. The mixes were prepared with a constant 50% content of S, while the remaining 25% was replaced with FA, D, or OP, as summarized in Table II. This ternary design approach facilitated the systematic variation of individual aluminosilicate source precursors' effects on the matrix evolution and ultimate composite behavior.

TABLE II. MIXTURE PROPORTIONS OF GM (kg/m³)

Mixture	OP (kg/m³)	D (kg/m³)	FA (kg/m³)	S (kg/m³)	Na_2SiO_3 (kg/m³)	NaOH (kg/m³)	Sand (kg/m³)
50S25FA25D (0.7)	0	100	100	200	186.67	93.33	1000
50S25FA25OP (0.7)	100	0	100	200	186.67	93.33	1000

All the precursor materials were oven-dried, crushed to fine particles, and then sieved to a particle size less than 90 µm to promote a uniform dispersion, enhance reactivity, and allow consistent surface availability within the mix. For the chemical activation, a binary alkaline solution comprising a 2:1 mass ratio of 12M NaOH and Na_2SiO_3 was selected to provide a high level of alkalinity and high silicate content necessary to create strong geopolymerization. The Na_2SiO_3 solution used as an activator had an Ms = SiO_2/Na_2O of 3.29, with a total solid content of approximately 35.5 wt.% and a specific gravity of 1.45 g/cm³ at 20 °C, ensuring a consistent silicate availability and gel formation across all mixtures. The liquid activator was added with an A/B ratio of 0.7, and uniform binder saturation was applied to all mixes. After considering the water content in the sodium silicate solution, the effective water-to-binder ratio came out to be around 0.28, providing sufficient workability while not precluding the evolution of a dense and mechanically adequate matrix.

Following homogenization, fresh GMs were compacted by being poured into prismatic molds with strict adherence to the TS EN 196-1 standards and lab best practice to achieve reproducibility and exact dimensions. Two highly purified copper electrodes were fixed symmetrically along opposite internal vertical mold faces with an imposed inter-electrode distance. These were seated flush on internal walls and mechanically held in place for stable positioning during casting. The electrode ends extended through the mold body, allowing external attachment to a programmable sinusoidal AC power source with variable output voltage.

The casting was carried out in two stages. First, half the mortar volume was poured and compacted for 30 s on a calibrated vibrating table (amplitude about 0.4 mm). This step ensured an even particle distribution and the removal of the entrapped air. An additional layer was poured before a 45–60 s compacting cycle was carried out, ensuring complete matrix consolidation. Each top surface was hand-leveled by a stainless-steel trowel shortly after casting, ensuring a level surface and dimension control without applying excessive pressure, which could disrupt the internal structuring of the matrix. The molds were then sealed with a vapor-permeable thick plastic membrane to retain the internal moisture and prevent premature drying or environmental carbonation from entering the fresh mortar, especially at its early initial setting stage and geopolymerization period.

The ambient curing involved placing covered molds within a humidity-saturated chamber at a constant 23 ± 2°C, ≥95% RH for 24 h. After 24 h, the samples were demolded and transferred to a room-temperature-controlled laboratory (23 ± 2°C, 50% RH) environment for continued hydration until the test ages. In contrast, under the applied thermal curing procedure, the covered samples were undisturbed for 24 h, whereupon they were demolded and transferred into a pre-heat-treated laboratory convection oven maintained at 80 ± 1°C. The oven was shut off upon curing, leaving the samples to cool naturally for at least 3 h to avoid the thermal shock before being stored under ambient conditions.

In EC mode, immediately after casting, copper-electrode-embedded samples were attached to a sinusoidal Alternating Current (AC) power unit with constant voltages of 30 V, 40 V, or 50 V, depending on the particular experimental group, as seen in Figure 1. AC generates volumetric heating through Joule dissipation ($Q = I^2R$), with distributed resistive heat generation supported by fresh geopolymer matrix ionic conductivity. In contrast to DC systems, AC operates at 50 Hz, preventing the electrode polarization, directional ion migration, and localized electrochemical degradation, ensuring uniform electrochemical balance and heat. The internal temperatures were continuously monitored using centrally embedded K-type thermocouples, with peak core temperatures ranging from 70°C to 85°C, depending on the voltage and time. Concurrently, the current flow tapered off as the ionic mobility was reduced due to gelation, reflecting progressive polymerization and establishing a natural feedback heat loop. After the voltage was removed, the samples were passively cooled in the mold at ambient temperature before demolding, allowing gradual thermal equalization and reducing the risk of internal microcracking.

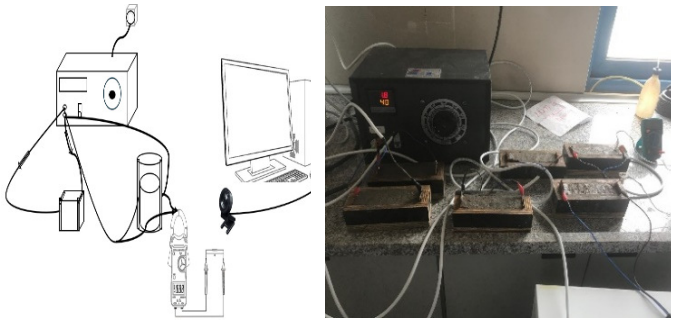

Fig. 1. EC setup used in the experimental study.

Physical and mechanical tests were conducted on 40 mm × 40 mm × 160 mm prism-shaped samples. Three similar samples (n = 3) were prepared and tested for a specific mix design and curing environments, enabling statistically significant comparisons.

The water absorption was measured according to ASTM C642. The apparent porosity and bulk density were measured using oven-dried, saturated-surface-dry, and immersed sample masses, allowing an accurate determination of the matrix compactness and pore volume. The capillary absorption was then tested according to ASTM C1585, where the lateral surfaces of the dried prisms were coated with epoxy and the bottom surfaces were subjected to 3 ± 1 mm of deionized water; mass increments were recorded at 1 min to 24-h intervals from where the sorptivity index (I-value) was calculated by normalizing the cumulative sorption with the square root of time to fulfil the one-dimensional flow requirements. Upon the completion of physical testing, the flexural strength was determined based on ASTM C348 using a three-point flexural setup on a 100 mm span sample, utilizing a loading rate of 50 ± 10 N/s.

The Compressive strength was assessed on fractured halves under a uniaxial loading of 2.4 ± 0.2 kN/s, according to ASTM C349 procedures. Physical and mechanical examinations were carried out routinely after 7 and 28 days of curing to simulate the early age formation and longer-term maturation within various activation regimes. The microstructural features were also studied using SEM, in accordance with ISO 16700:2007, where core region gold-sputtered fractural surfaces were examined with 15–20 kV accelerating voltage to witness the gel morphology, remnant phases from precursors, and interconnecting pore features, as depicted in Figure 2. Concurrently, the phase identification and crystalline evolution were investigated using XRD in accordance with ASTM C1365, with Cu-Kα radiation of $\lambda = 1.5406$ Å, a scanning range of 2θ: 5°–70°, and a step size of 0.017° to determine the effects from the aspects of the precursor chemistry and curing regimes on the geopolymeric matrix.

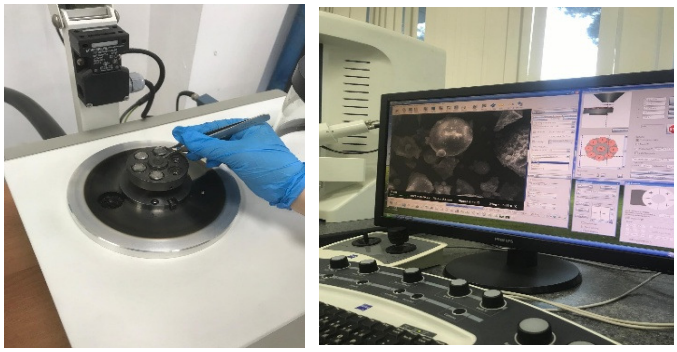

Fig. 2. Microstructural analysis of GMs.

III. RESULTS AND DISCUSSION

A. Mechanical Properties

Under benchmarking conditions, other control combinations of OP as a partial D substitute (i.e., 50% S + 25% FA + 25% OP) were similarly synthesized to explore the mechanical viability of the inert filler-type precursors within the ternary geopolymer matrix. While their structural correspondence to the other series resided in the mix ratio and activator content, these OP-based series showed much lower performance. The compressive strengths only averaged around approximately 10.3 MPa on ambient curing and up to approximately 20.0 MPa on thermally curing for 28 days at 80 °C. These values signified the minimal level of inherent reactivity and zero contribution to the gel formation of the OP over reactive D, which tends to support dissolution-controlled gel nucleation. Therefore, the attention shifted to the 50S25D25FA series, which exhibited a much better matrix evolution and mechanical gain within various curing environments.

A combined bar-line chart with two Y-axes and error bars provides an enhanced visualization of the mechanical development of the 50S25D25FA series, highlighting the relative influence of the curing temperature and duration on the compressive strength and flexural strength, respectively. Figure 3, which represents the compressive strength behavior over 7 and 28 days for ambient curing and 80 °C thermal curing regimes, shows a clear upward trend with both the curing duration and higher temperature. Whereas, on day 7, the ambient curing sample yields 15.98 MPa, which accounts for the developed constraint of the early-age geopolymerization undergone under ambient temperature, especially for Class F FA (25%) and D-based (25%) post-combustion geopolymerization. Both are documented to have limited extents of calcium content and slow functionalities under ambient environments. While D, despite its high content of amorphous silica, requires extensive activation energy from the alkali to open up its porous body and increase the dissolution of the silicate chains, Class F FA, with a high level of SiO_2+Al_2O_3+Fe_2O_3 (approximately 89.75%)-rich content, possesses a latent binder, which relies on an extensive level on external energy inputs to get activated. Therefore, the moderate strength value here closely aligns with the inherent chemistry of THE slowly reactive, low-calcium materials.

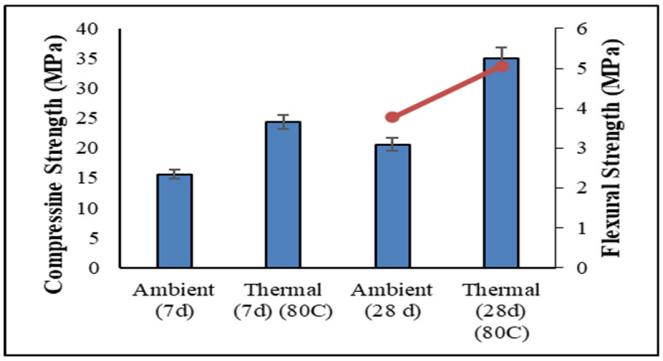

Fig. 3. Effect of ambient and thermal curing on the compressive strength of GMs.

In comparison, the level of compressive strength was found to be 24.34 MPa at 7 days for the thermally cured samples, which constitutes a considerable increase, a gain of 52.6% compared to ambient-curing. This behavior is closely related to the elevated content of CaO of the granulated blast furnace S (50%), which, being exposed to high temperatures, rapidly dissolves as an alkaline medium to create C-A-S-H gels, with limited formation of N-A-S-Hs from FA and D.

Polycondensation accelerates under the thermal regime, and the geopolymer gel network develops more homogeneously and densely. This translates to the possibility of elements being cast, with this mix design reaching a structural loading capacity within a much shorter period, especially when applicable to precast use or accelerated module casting. Narrow error bars indicate repeatability and mechanical development consistencies, and their presence reinforces the reliability of the mix within thermally controlled environments.

At 28 days, the compressive strength of the ambient cured samples rises to 20.59 MPa, representing a 29.1% increase from its 7-day value. This indicates the gradual but steady reaction of unreacted aluminosilicates with time, a characteristic of FA-based materials. Nevertheless, the gain is relatively moderate compared to the thermally cured sample. Its thermally-cured counterpart achieves a compressive strength of 35.03 MPa, translating to a 46.3% increase compared to its 7-day thermal strength and a 72.9% superiority over the 28-day ambient curing strength. This shows that the thermal curing produces more than twice the strength of ambient curing at early ages and remains superior at later ages.

Also, the net gain in compressive strength from the 7-day ambient curing to the 28-day thermal curing is 19.4 MPa, corresponding to a 123% gain in strength. This is especially important for the structural members, where the curing duration and reliability are limited, as they provide a way to improve the material utilization and shorten the construction cycle. The trend remains consistent even for the flexural strength, often a better indicator of the matrix continuity and microcrack resistance. At 28 days, the flexural strength increases from 3.77 MPa (ambient curing) to 5.06 MPa (thermal), reflecting a 25.5% improvement. Although not as dramatic as the compressive strength gains, this still represents a meaningful enhancement in the load distribution and energy absorption potential. However, a deeper inspection of the flexural strength-compressive strength ratio reveals a reduction from 0.195 (ambient curing) to 0.142 (thermal), suggesting that while thermal curing enhances the strength, it may also lead to a relative loss in ductility. This is a known effect of the thermally matured geopolymer gels, where the increased cross-linking and phase crystallinity restrict the crack bridging and flexibility. The matrix becomes stronger, but also stiffer and potentially more brittle. This trade-off is significant in practice and may necessitate mitigation strategies, such as short fiber addition (e.g., PVA, basalt, or polypropylene) or particle gradation optimization to restore the fracture energy without compromising strength.

From a material science point of view, the improved performance with thermal curing is due to various synergistic processes. First, the increased dissolution rates of the calcium, silica, and alumina components within the alkaline activator allow for a more complete reaction formation within the gel phase. Secondly, higher temperatures encourage the refinement of pores, minimizing the extensive capillaries and boosting the mechanical entrainment locking. Thirdly, D's porous nature facilitates better internal curing and activator solution retention, enabling more uniform reaction fronts. These reactions cumulatively produce a compact, more stable microstructure on which the mechanical failure relies under compressive and flexural loading. Also, the S component with elevated reactivity brings about early-stage hardening, while the FA achieves long-term contribution with latent reactivity [22-25]. This two-phase mechanism is key to the long-term strength stability observed. Statistically, the gain rate of the compressive strength under ambient curing from 7 to 28 days is in the order of (20.63 - 15.98) / 21 ≈ 0.22 MPa/day, whereas with heat curing, it is (35.67 - 24.39) / 21 ≈ 0.54 MPa/day, offering a 145% higher strength gain rate with the heat treatment. This reinforces the fact that not only the ultimate strength achieves higher values with heat curing, but also the strength gain duration is reduced, which is a robust advantage for rapid field deployment. For high-production needs, this could lead to faster plant turnover, reduced formwork holding time, and overall cost savings through shorter building cycles.

In contrast, there are logistical and energy-based difficulties with thermal curing, especially with in-situ uses for which the curing chambers or controlled environments are impractical. Hence, the use of thermal regimes must balance the mechanical advantage with the operational practicality. With exceptional cases, like prefabricated panels, geopolymer tiles, insulated wall sections, or prefabricated components. But with large-scale poured uses within the field, there could be ambient curing with long durations or hybrid curing strategies (e.g., step-wise thermal activation) to achieve better-balanced results.

The compressive strength development for the 50S25D25FA series subjected to EC under three voltage regimes of 30 V, 40 V, and 50 V is portrayed in Figure 4. Under 30 V, the compressive strength develops steadily from a 1-h mean of 21.49 MPa to 27.65 MPa at 24 h—a 28.7% net gain over the 23 h, reaching 1.55-times the ambient curing benchmark and 0.78-times the thermal milestone. The hourly rate of development in this series averages 0.27 MPa/h, a consistent but time-consuming strengthening trajectory. With no evidence of a reverse progress trend, 30 V appears to generate enough internal heat to activate the mobilization of the silicate and aluminate for the polycondensation reaction, but capped sufficiently not to lose water and produce shrinkage or develop a microcracking behavior. This suggests a high endurance for extended curing duration and low volatility in performance features, which are extremely attractive for field utilization with the requirement for gradual, homogeneous gain in properties. In contrast, the 40 V regime has a rapid and peaked development curve, peaking at a maximum mean compressive strength of 31.34 MPa at 4 h of age, corresponding to 1.75-times the ambient curing and 0.88-times the thermal maximum, and 20 h ahead of the 30 V maximum, representing a roughly 5.5-times enhancement in the efficiency of the strength acquisition. The 6.80 MPa cumulative gain over the 1-4 h period, or 2.27 MPa/hour, outpaces every other condition over the same period, but from 4-24 h, a drop of 15.6% occurs, with the strength falling back to 26.42 MPa, below the 4-h maximum and 0.74-times the thermal maximum.

This biphasic response implies that although 40 V maximizes the window for initial activation, through rapid ionic transport and exothermic reaction augmentation, it also risks initiating unwanted secondary processes, such as water

depletion and pore destabilization if prolonged beyond reasonable bounds. These 4 h mark an inflection point, representing the energetic crossover beyond which the rate of damage accumulation exceeds the gain in strength, making the regime's narrow but valuable processing window apparent. In an industrial context, 40 V_{4h} achieves 88% thermal curing in 14% of the time, representing an unparalleled benefit in precast, fast track, or energy-conservation construction regimes, with the caveat being the need for curtailing post-peak retrogression through rigorous management of the detailing process. The 50 V regime, while providing the highest nominal energy input, underperforms quite seriously in all durations. From a starting point of 20.47 MPa at 1 h (only 1.15-times ambient base and 0.57-times thermal maximum), the values oscillate moderately before reaching 18.39 MPa at 24 h, a 1.03-times increment above ambient curing and 0.51-times of thermal strength, and a complete 33.5% less than 30 V_{24h} despite the 67% increased voltage. This inverted voltage–mechanical relation demonstrates how the over-electrical stimulation causes a fast, uncontrolled heat buildup, leading to accelerated internal drying, cracking gel continuity, and resulting in thermal stress concentration domains in localized regions. Since the main effect is a negative strength change of -2.08 MPa from top to bottom, there is a limiting voltage value for safe GM curing at 50 V.

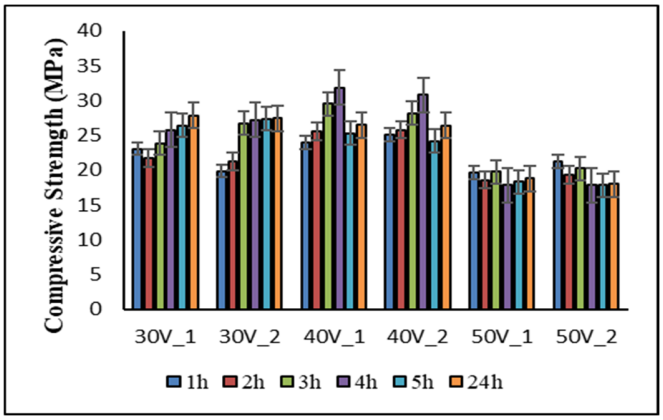

Fig. 4. Comparison of compressive strengths of GMs under 30 V, 40 V, and 50 V electrical curing for 1–24 h.

Pragmatically, while 30 V and 40 V have linear or peaked efficiency curves, 50 V has a destabilizing one in which the imposed energy overwhelms the internal water and by-product diffusion capacities, resulting in geopolymerization progression in a spatially inhomogeneous manner, as also in the disintegration of the prepared microstructure. Furthermore, in terms of the measure of volumetric efficiency in returning the voltage unit for the return obtained (MPa/V), 40 V_{4h} provides 0.78 MPa/V, and 30 V_{24h} provides 0.92 MPa/V. In comparison, 50 V_{24h} falls to 0.37 MPa/V, indicating that 30 V continues to be the most energy-efficient system, though slow, while 40 V is the most rapid, and 50 V is a structural waste. By further extension, the net strength-duration productivity metric places 40 V_{4h} at 7.83 MPa/h total, practically 3-times greater than the 1.15 MPa/h of 30 V_{24h}, and more than 10-times greater than the 0.77 MPa/h of 50 V_{24h}. Measured in terms of a thermal benchmark percent attainment by the hour, 40 V_{4h} registers 22%/h, contrasting with 30 V_{24h}'s 3.2%/h, and the 2.1%/h of 50 V_{24h}.

These normalized values reaffirm that all three voltage regimes can yield satisfactory early-age strength with ambient conditions. Still, only 40 V achieves genuine parity with thermal curing in a small fraction of the time, assuming a tightly controlled duration, avoiding degradation. While 30 V's linear trend and 40 V's parabolic climb-fall contrast with 50 V's plateau, the resulting performance topology provides a voltage-time envelope onto which the contours of industrial-scale geopolymerization can be mapped [26-28].

Figure 5 displays the flexural strength performance for the 50S25D25FA series subjected to EC at three voltage regimes, 30 V, 40 V, and 50 V. Under exposure to externally imposed 30 V, 40 V, and 50 V voltages over 1-24-h periods, the flexural strength profile appears as a diagnostic response encoding the internal state of the matrix in terms of the degree of gel formation, crack resistance, heat tolerance, and mechanical ductility.

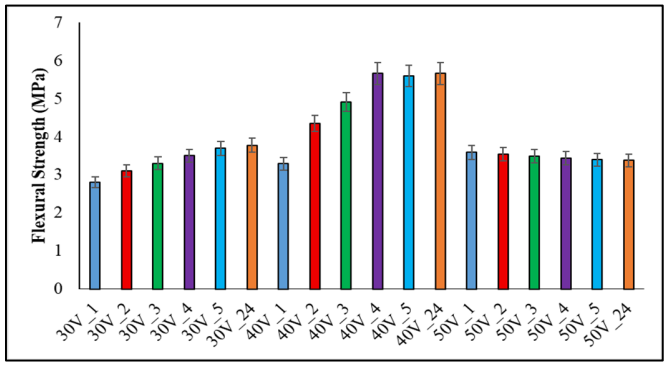

Fig. 5. Comparison of flexural strengths of GMs under 30 V, 40 V, and 50 V electrical curing for 1–24 h.

Unlike the compressive strength, reflecting the bulk cohesion, the flexural strength is instantaneously determined by the material's tensile stress-resisting ability over its surface-most fibers, rendering it highly sensitive to surface gel continuity, microcracking, and drying-related shrinkage. Such sensitivity makes flexural strength the perfect measure for determining the real-time success of EC conditions and for encoding the subtle behavior of alkali-activated binders under controlled electrical stimulation. At 30 V, the flexural strength values are at approximately 2.80 MPa (avg) and trend towards approximately 3.78 MPa at 24h, representing a cumulative development of approximately 35% over 23 h. This sustained increment, in the form of non-retroversion, reflects a controlled and internally consistent gelation process—presumably dominated by equilibrated silicate dissolution, consistent retention of water, and unintermitted N–A–S–H gelation in the surface tension zones in the prism of the mortar. The flexural strength-compressive strength ratio in this condition also remains moderate (approximately 0.137), implying that the matrices prefer a compressive over a tensile bearing of loads, a

characteristic condition in slow-reacting, low-energy geopolymerization when tensile regions lag in densification.

Nevertheless, its final proximity towards the ambient curing flexural strength reference (3.87 MPa → 97.7%) and decent level of thermal standard compilation (5.44 MPa → 69.5%) also implies that with adequate curing time, low voltage regimes are capable of supplying reference-level mechanical performance in flexure as well. The most dramatic improvement occurs under the 40 V regime, where the values of flexural strength go up from approximately 3.29 MPa at 1h to a maximum of 5.66 MPa at 24h, representing a 72% enhancement and topping the thermal benchmark of 5.44 MPa by 4%, with 46% better than ambient flexural strength. However, this extraordinary performance is as much a function of voltage magnitude as an energetic balance. The 40 V supplies a sufficient internal thermal field for the rapid mobilization of dissolved constituents, with internal humidity retention avoiding associated first-stage gel brittleness. The flexural strength-compressive strength ratio peaks at approximately 0.200, marking a matrix that can tolerate high tensile stresses about compressive stresses—i.e., a tough, pliable microstructure with increased crack-bridging capabilities. Consistent with the proposition that 40 V allows maximum polymeric chain extension and polymeric chain extension/cross-linking in a critical 3–4-h period, with little payoff for increased curing beyond, the rate of flexural strength gain at 40 V for 1–3h (approximately 0.7 MPa/h) is 16-times better than for 30 V, and nearly 10-times better than for 50 V, affirming the superiority of the thermal-kinetic synchronization over pure duration.

In contrast, the 50 V regime demonstrates the ill effect of overactivation. The flexural strength reaching a maximum early on (approximately 3.59 MPa at 1 h) and declining towards approximately 3.38 MPa at 24h provides the worst endpoint and a regressive trend, or evidence of thermally driven material instability in the matrix. Its internal microstructure must have suffered excessive capillary pressure due to unregulated water evaporation, with pore coarsening and softened gel interfaces as a result. Even though it provides the most electrical input, its flexural strength-compressive strength ratio (approximately 0.184) stems not from an enhanced tensile performance but from an anomalously reduced compressive strength. Furthermore, its efficiency in flexural strength by voltage (0.067 MPa/V) and by hour (0.141 MPa/h) is the lowest among all regimes, confirming that using higher voltage without process regulation, wastes energy and deteriorates the mechanical integrity. These findings uphold the "activation ceiling" principle of geopolymer electrocuring: overrunning the thermal-mass buffering limit of the system speeds up destruction rather than development.

Examining these trends in energetic metrics further supports the technical limits. The 40 V_{4h} yields approximately 5.66 MPa flexural strength and approximately 28.25 MPa compressive strength, providing 0.142 MPa/V and 1.415 MPa/h flexural strength outputs—significantly better than 30 V and 50 V. In contrast, 30 V_{24h} competes in electrical economy (0.126 MPa/V), but not in time efficiency (0.157 MPa/h), while 50 V does poorly in both categories. These outputs have significant scaling and implementation ramifications. The 40 V curing is most suitable for precast geopolymer applications in which strength is essential, while 30 V suits off-grid or cost-constrained situations. Furthermore, the strength-per-energy ratios indicate that real-time feedback-controlled curing may be able to vary voltage to track the response rate curves, maximizing the development of flexural strength without exceeding the safe thermal thresholds. Mechanistically, such outcomes represent the intrinsic response of alkali-activated matrices under localized internal heating in the initial stage. Thermally accelerated dissolution of the reactive filler phases, the FA, and the S release an alkaline medium with high concentrations of Na^+, OH^-, and soluble Si ions. Under the ideal voltage (i.e., 40 V), this medium supports a rapid nucleation and subsequent fast growth of aluminosilicate gels, which interconnect without entropic dehydration in the early stages of formation. Since the flexural zones are most prone to shrinkage cracking, the sustained internal humidity under 40 V prevents the tensile brittleness, maintaining continuity in the gels throughout tension-dominant surface fibers. The 50 V, on the other hand, induces explosive water evaporation before the polymerization of the matrix, with the attendant formation of voids, weak interfaces, and patterned brittleness in the final product.

The flexural strength-compressive strength ratio also assists in deciphering the structural behavior. Increased ratios suggest ductile matrices with the potential for post-peak load distribution, while low values indicate monolithic, brittle failure. The 40 V's high Flexural strength-compressive strength ratio (approximately 0.20) suggests the potential for greater fracture toughness, while the 30 V's low ratio signifies a stiffer, more elastic behavior. From the engineering perspective, this influences the response of the geopolymer components to flexural-prone stresses, like those in beams, panels, or slabs. The high flexural strength with corresponding compressive strength provides both shear and tensile stability, a requirement for seismic or impact-prone structures. Ultimately, this in-depth flexural analysis illustrates clearly that GMs are not passively reactive to electrical curing—they require precise congruity between voltage, duration, and internal hydration kinetics. Optimal strength, efficiency, and structural integrity are found at 40 V over a 4–6 h time period. This condition satisfies not only the mechanical thresholds, but also the energy-performing balance, curing cycle reduction, and optimization toward crack-resistance [29-31].

B. Physical Properties

With the principles of multivariate statistical diagnostics, the bidispersion matrix has emerged as a high-dimensional graphical system capable of resolving the latent inter-variable relationships in an effort to determine the densification trends, inverse porosity-density trends, and water transport behavior of the complex binder systems. The pair-scatter matrix in Figure 6 shows the three-dimensional relationship between the water absorption, apparent porosity, and bulk density in GMs cured under five different regimes: ambient curing, thermal activation, and electro-curing at 30 V, 40 V, and 50 V. By facilitating a simultaneous visualization of the parameter interaction as well as of the inter-series contrast, this matrix is

useful not just as a diagnostic chart of capillarity-mediated performance, but also as an evaluation tool of the efficiency of unconventional curing regimes in designing the pore hierarchy of GMs.

Every point in the matrix represents a unique microstructural signature, and the dispersion of these points along the scatter-planes reflects uniform patterns that correspond with the basic principles of densification, ionic mobility, and the reaction kinetics of geopolymer chemistry.

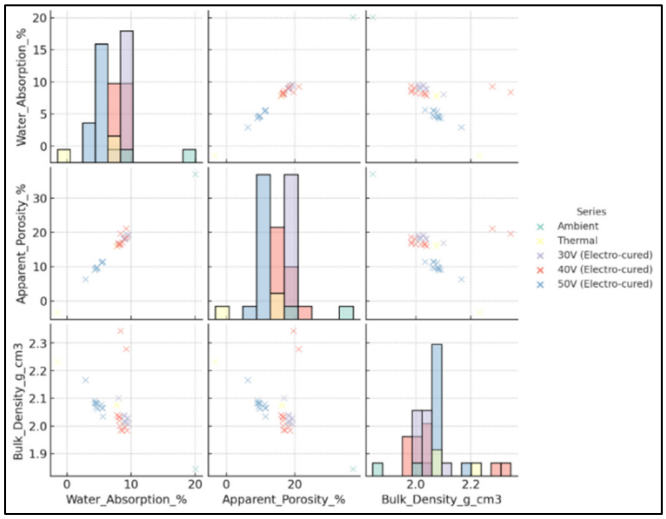

Fig. 6. Pairwise distribution plot comparing water absorption (%), apparent porosity (%), and bulk density (g/cm³) of GMs subjected to different curing regimes: ambient, thermal, and EC at 30 V, 40 V, and 50 V.

Ambient-curing samples (marked green) always lie on the outer edges of the water absorption–porosity curve with values commonly above 35% for porosity and 20% for water absorption. The last values reflect the characteristics of an extremely poorly developed matrix that is probably an effect of geopolymer incompleteness in the absence of an external activation stimulus. In such systems, the limited dissolution of the precursor aluminosilicates (e.g., S, FA, ceramic powder) leads to incomplete geley formation, improper chain-linking of silico-aluminate units, and the preservation of the interconnectivity of capillary-sized pores, which maximizes the uptake of water besides causing a compromise of the final composite's chemical and structural resistance. This cluster possesses the lowest bulk densities with values typically below 2.00 g/cm³, reinforcing the visible presumption of the microstructure's open-celled, loose, poorly refined nature. Conversely, the thermal curing samples (yellow) from high-temperature exposure commonly in the 80°C range show considerable departure from ambient conditions. The samples congregate near 15–17% porosity levels and 7–9% absorption rates, with bulk density increasing to some 2.10 g/cm³. This is consistent with established literature findings, according to which the thermal input speeds the dissolution of aluminosilicate ions, promotes polycondensation reactions, and promotes the formation of a denser N-A-S-H or C-A-S-H gel network.

The thermal curing trajectory, therefore, produces tighter microstructural packing, less porosity in the gel phase, and fewer pathways for water accessibility. The scatter matrix clearly positions thermal curing relative to the three electro-curing methods, allowing a direct side-by-side comparison of curing-induced performance gradients. While the heat activation is always beneficial, especially for thick-section components or limited resource situations, its advantage is seen to level off compared with higher-efficacy EC modalities. The EC samples of 30 V, 40 V, and 50 V are especially enlightening in this matrix. The 30 V samples start to break from the thermal group with porosities of around 15% and absorption around 6–8%. While less than optimal, these numbers already point to an improved ion mobility along with greater uniformity of gelation in the presence of the applied electric field. The transformation in the 40 V and 50 V samples is the most striking, which group closely around the 10–12% porosity value with the absorption falling to 4–6% and the bulk density well over 2.10 g/cm³, consistently. The visible compactness of the 50 V group on all scatter-planes signals not just advancing densification, but minimal variability in the dataset, as well, which is a sign of an efficient, repeatable curing process.

These results strengthen the hypothesis that electro-curing enhances the electrokinetic ion migration of ions, like Na^+, Ca^{2+}, and OH^-, thus facilitating a rapid nucleation and uniform distribution of the geopolymer gel phases. This leads to the sealing of microcapillary channels and an accompanying drastic decrease in interconnection porosity, while maintaining or improving the overall matrix cohesion. In addition, the inverse correlation between the bulk density and capillarity indicator metrics (apparent porosity and water absorption) in all curing series provides additional substance to the interpretation.

The increasing bulk density is associated with decreasing water absorption and porosity—a trend that is not merely correlational but causative. A higher density is indicative of less space available for pores to form within the material, better packing of the reaction products within the intermicellar spaces, and enhanced connectivity of the latter within the gel phase. All these lead to decreased permeability and increased durability in hostile environmental service conditions. This trend is particularly noted in the EC-series. Thus, these techniques do more than merely densifying the matrix, as they actively rearrange the inner pore network in ways that the ambient and thermal curing cannot imitate. In addition, the scatterplot indicates that the thermal curing and 40 V electro-curing yield nearly coincident performance envelopes. Hence, it is possible to envisage substituting the thermal curing with electro-curing in situations where the thermal energy is impractical or economically inadvisable. Notably, this matrix highlights the multi-dimensional nature of the curing effects—not just do the electro-curing regimes exhibit reduced porosity, but also stabilize the microstructure, as reflected in the less scattered and closer grouping of the data points for each level of curing voltage [31-35]. This indicates process reliability and scalability, which are critical in construction use.

The ambient series shows the highest spread, indicative of the stochastic nature of hydration with limited interconnectivity

of the gel phase and possible vulnerability to environmental factors, like humidity, temperature oscillations, and carbonation. The plot again establishes that the enhancement in the property of resistance to water does not compromise density or compaction, but instead shifts beneficially with higher curing voltages for the three parameters.

In multi-performance-demand-driven material systems, such as GMs, that should be best combined for mechanical strength, durability, and microstructural compactness, the conventional single-variable ranking methods are insufficient for overall evaluation. Such systems tend to have inherent compromised relationships, so that the optimization of a specific criterion, such as compressive strength, can be a negative for others, such as porosity or water absorption. In an attempt to explicitly capture and deal with such interdependencies, an MCDM approach was designed, which can be employed for the consolidation of various quantitative indices of a heterogeneous nature into a unifying, rational form for decision making. In this methodology, the Weighted Sum Model (WSM) along with the Weighted Product Model (WPM) were selected, specifically due to their interpretability, computational advantage, and record of application for engineering-based ranking of performance. WSM validates a linear combination of weighted criteria, which yields an explicit solution of compromise, whereas WPM emphasizes the geometrical interplay of variables, which recognizes the balance of performance through multiplicative normalization. However, the models are themselves deterministic and seriously limited when faced with zero or near-zero normalized values, which can distort the resulting ranking even with balanced system-wide performance.

To offset this structural inflexibility, fuzzy logic was introduced to the decision procedure in the form of an additional inferential layer. According to Zadeh's fuzzy set theory, the approach accepts degrees of membership as well as partial satisfaction of criteria, which induces an interpretive flexibility better suited to human thinking than the binary models of appraisal. Fuzzy logic can accommodate ambiguities and marginally conflicting performance through the transformation of normalized values to graded scores, therefore enabling a softer effect of localized weakness and a more subtle recognition of steady, moderate performance on all indicators. This feature is particularly useful for the geopolymer optimization problem, where one curing regime may not be a top performer for every parameter, and field application may judiciously opt for regimes of well-balanced characteristics rather than regimes of extremal polarization.

Fuzzy logic was chosen over hierarchical methods, such as AHP or ANP, which, though methodology-rich, are heavily dependent on subjective pairwise ratio scale comparisons and consistency matrices. These are better suited for expert-opinion-driven situations than for data-rich situations, such as the present study, where the experiment outputs are given and the inter-criteria autonomy is reasonably taken for granted. Fuzzy logic, however, works with normalized empirical data straightforwardly, eliminates the mediator of subjective weighting itself, and gracefully coexists with the objective framework offered through the classical MCDM models. By unifying deterministic precision with perceptual variability, a hybrid analytical method yields a robust, interpretable, and context-sensitive ranking of curing regimes. It delivers the most technologically performant alternative while also revealing the subtle advantages of intermediate regimes, thus giving a superior basis for material choice for practical alkali-activated binder uses [36-39].

To objectively rank the five distinct curing regimes in terms of their overall performance in GMs, a dual-tier decision-making approach incorporating both classical MCDM and fuzzy logic scoring was implemented, as presented in Table III. This hybrid evaluation strategy aimed to capture each regime's quantitative robustness and qualitative responsiveness under a consistent matrix of performance indicators.

The analysis focused on six key performance metrics: compressive strength, flexural strength, flexural strength-compressive strength ratio, bulk density, water absorption, and apparent porosity. These parameters were pre-processed using min–max normalization, with cost-type criteria (water absorption and apparent porosity) inverted before aggregation to ensure directional coherence in the scoring. Within the MCDM framework, two classical models were employed: the WSM and the WPM. The assigned weights were 0.25 for the compressive strength, 0.20 for the flexural strength, 0.15 for the flexural strength-compressive strength ratio and bulk density, and 0.125 for the water absorption and apparent porosity, reflecting the dual importance of the mechanical integrity and durability in geopolymeric systems.

In the WSM ranking, the 40 V electrothermal regime achieved the highest overall score of 0.857, followed by thermal curing (0.779), 50 V (0.496), 30 V (0.488), and ambient curing (0.193). The exact hierarchy was confirmed in the WSM ranking positions: 40 V (1st), thermal (2nd), 50 V (3rd), 30 V (4th), and ambient (5th). These scores reveal that the 40 V electro-curing delivers superior aggregate performance, outperforming the thermal benchmark across all weighted performance indicators. The WPM model, which multiplies normalized scores raised to their respective weights, further validates these trends. The 40 V again topped the chart with a WPM score of 0.840, followed by thermal at 0.701. Notably, both the 30 V and 50 V yielded WPM scores of 0.000, indicating the presence of zero-normalized values in at least one performance parameter.

TABLE III. MULTI-CRITERIA AND FUZZY DECISION ANALYSIS

Curing regime	Fuzzy score	Fuzzy rank	WSM score	WSM rank	WPM score	WPM rank
Ambient	0.202	5	0.193	5	0.000	4
Thermal	0.747	2	0.779	2	0.701	2
30 V	0.517	4	0.488	4	0.000	4
40 V	0.866	1	0.857	1	0.840	1
50 V	0.603	3	0.496	3	0.000	4

C. Microstructural Analysis

Penalizing their final ranking under the multiplicative scheme, ambient curing scored 0.000. Therefore, only thermal and 40 V successfully maintained a balanced performance

across all metrics, while the 30 V and 50 V were penalized for inconsistency. To extend beyond rigid MCDM frameworks, a fuzzy logic-based model was introduced wherein each criterion was treated with equal weighting, and the final fuzzy score was computed as the simple average of the normalized values across all six parameters. This approach sought to simulate the more nuanced, human-like perception of performance, whereby imperfect but balanced systems can sometimes surpass highly polarized ones. According to this fuzzy model, the 40 V again ranked 1st with a fuzzy score of 0.866, followed by the thermal (0.747), 50 V (0.603), 30 V (0.517), and ambient (0.202).

These results corroborate the MCDM findings but add necessary interpretive depth. For example, the 50 V improved from the 4th place in WSM to the 3rd in the fuzzy ranking, suggesting that its relatively high bulk density and low porosity still afford its moderate robustness despite the thermal damage. Similarly, 30 V's fuzzy score (0.517) remained stable but unimpressive, reflecting a conservative but unspectacular performance envelope. When breaking down the scores further, the WSM difference between the 40 V and 30 V was 0.369 (a 75.6% advantage), whereas in the fuzzy model, the score difference was 0.349 (roughly 67.5%). This repeated pattern of superiority reiterates that the 40 V represents an optimum crossover of strength, density, and durability characteristics, making it suitable for field-deployable alkali-activated applications demanding acceleration of performance and reliability. Conversely, the ambient regime was a constant last in all models, with the WSM (0.193), WPM (0.000), and fuzzy (0.202) scores reflecting a general inferiority by more than 75% concerning the leading performer, which points to the inadequacy of passive ambient curing in terms of creating dense and mechanically tenable matrices in alkali-activated matrices. The flexural strength-compressive strength ratio, a significant microstructural ductility and toughness determinant, also affected the fuzzy scoring. Even though the 50 V had a very high flexural strength-compressive strength ratio (approximately 0.184), its low compressive strength (18.39 MPa) and decreased flexural strength (3.38 MPa) affected its composite score. On the other hand, the 40 V not only had a high compressive strength (31.34 MPa) and flexural strength (5.66 MPa) absolute values, but it also had a desirable flexural strength-compressive strength ratio (approximately 0.201), which indicates a matrix of both stiffness and resilience.

SEM and EDS of the GMs show a systematic evolution of the gel morphology, particle dissolution, and matrix incorporation depending on the curing regime. Distinct textural features are observed for the ambient, thermal (80 °C), and electrothermal (40 V) curing conditions, as shown in Figure 7. For the ambient-curing sample, SEM reveals a chemically underdeveloped and fissured structure consisting mainly of sharp-edged, spherical FA particles, approximately 5-15 µm in diameter, loosely bedded within a wide, fibrous binder matrix, with extensive capillary voids of approximately 5–8 µm. These untransformed FA particles display their original glassy nature with no sign of pitting, rim leaching, or surface softening, and therefore confirm a negligible dissolution and no gel-phase anchoring. The EDS analysis within these areas would correspondingly yield high Si and Al peaks with negligible Na and/or Ca content, indicating their isolation from the geopolymeric reaction. Similarly, sharp-edged S grains within the ambient sample are introduced with a complete lack of extra-gel halos or surface transformation. EDS spots here would show high Ca and Mg, but no compositional gradings extending into the binder, and therefore confirm their inertia. The particles of D, recognizable as a result of their angular and microporous habit, exhibit preserved high textural definition and no surface encapsulation or smoothing, and therefore indicate that they have failed to participate to the matrix of silicates; the corresponding EDS data would show high Si with minimal Al and/or Na, and consequently a poor activation of their amorphous silica. The binder phase, whilst weakly evident within the fibrous aggregates, is highly discontinuous and exhibits a lack of amorphous contrast uniformity, lack of gradual greyscaping progressions, definition of ITZs, while the nodular gel structure identifies an ultramature matrix, therefore incapable of withstanding the anticipated stress transmission and/or long-term cohesive stability. The thermally cured sample exhibits a different morphological character, with a closely packed and uniform gel phase dominating the examination field, homogeneous greyscaping contrast, and complete elimination of the discernible boundary definition of the original precursors.

No spherically shaped FA remnants are seen, indicating complete dissolution and complete incorporation within the binder matrix. EDS spectra within these gel areas would have an equilibrium Si/Al/Na composition, characteristic of N–A–S–H gel phases, with moderate Ca levels within reaction-affected areas, corroborating (C, N)–A–S–H hybrid formation. S particles are partially decomposed and smeared out with neighboring amorphous material, consistent with open calcium release and secondary gel formation; EDS profiles would have high Ca/Si ratios (0.7–1.2), characteristic of well-formed regions of C–A–S–H. D is not seen any more as an individual phase, and thus it is assumed that their porous silica to have been dissolved and chemically bonded with the polymeric network; here, EDS would have elevated levels of Si with minor levels of Na and Al, indicating their contribution to compaction of the binder.

Overall field shows an indication of an absence of microcracking, delimited spots, and interface voids, and smooth nodular gel morphs consistent with the attainment of successful complete polymer main-chain formation and matrix maturity with compressive strength values above 35 MPa and porosity below 10%. In contrast, the EC sample with an anode voltage of 40 V shows an intermediate and strongly heterogeneously developed microstructure with, on one hand, simultaneous evidence of partial activation and local over-curing. Particles of FA frequently exhibit partial surface destruction with softened contours, pitting, and incomplete rim formation, indicating selective dissolution according to their positions concerning current paths. EDS mapping over such particles exhibits marginal incrementations of diffusion of Na and Al from adjacent areas indicating initiation of the geopolymerization reaction but lacking time or energy to achieve complete reaction.

S particles also exhibit variable reaction levels with some exhibiting signs of interface dissolution and gel film formation

while others remain textureurally distinct; EDS over these areas exhibit sudden Ca transitions and interrupted formation of C–A–S–H. While localized amorphous gel bridges are observed joining some precursors, most of the matrix is cracked and discontinuous, and porosity is very variable (estimated 15–20%) with a distance from the current path. Non-uniformity of ITZ formation and stochastic densification gradients suggest that whilst electro-curing induces partial reaction and matrix stiffening, spatially non-uniform current distribution induces phase segregation, microstructural asynchrony, and mechanical instability.

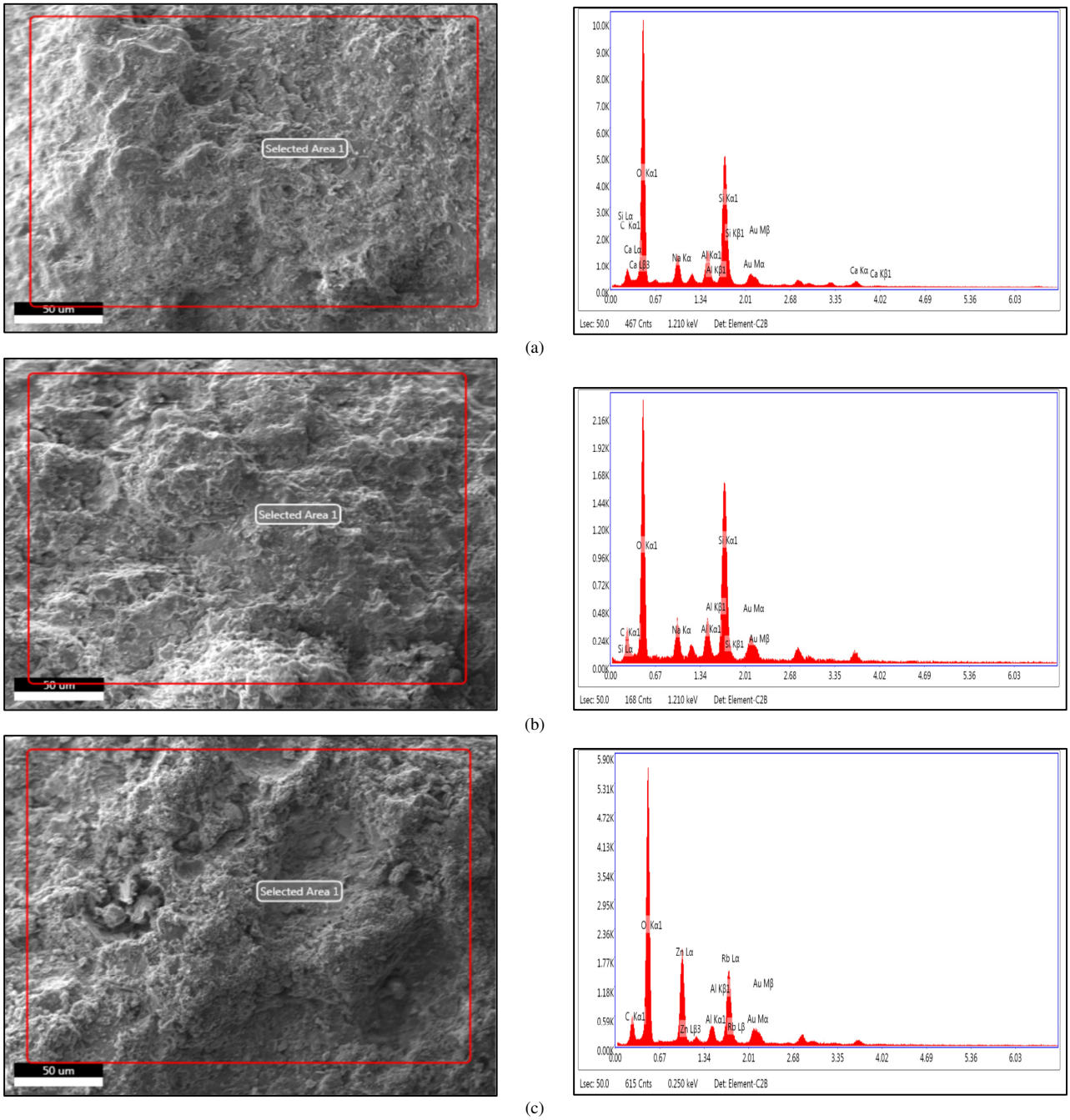

Fig. 7. SEM of GMs: (a) ambient curing; (b) thermal curing (c) electrical curing.

XRD of the GMs—involving equal contributions of S, FA, and D—comprises an overwhelming, diffuse hump centered between ca. 25° and ca. 35° 2θ, characteristic of the amorphous aluminosilicate gel phase synthesized during geopolymerization (Fig. 8.). This amorphous halo, extending optically between approximately 22° and 38° 2θ, is characteristic of N–A–S–H and C–A–S–H-type gels, developed during the dissolution and re-polymerization of the reactive

silicates and aluminates under alkaline conditions. The absence of sharp, predominating crystalline peaks within this range confirms an effective transformation of major fractions of reactive FA and S phases into the amorphous binder, successfully forming the geopolymer network. However, the XRD spectrum continues to signify superposed minor crystalline reflections, testifying to the survival of unreacted or semi-reacted phases. Most intensive among these are the ones found to appear at approximately 26.6° 2θ, assigned to quartz (SiO_2)—presumably retained both from FA and D—and another evident one set at approximately 27.9° 2θ, assigned to mullite ($3Al_2O_3 \cdot 2SiO_2$), a thermally stable crystalline phase inherited from the source FA.

These reflections are relatively sharp but moderate to low in intensity, testifying their presence from small but highly structurally resistant amounts of alkaline depolymerization. Additionally, weaker peaks observed to appear at approximately 36.5°, 50.1°, and 59.9° 2θ may correspond to gehlenite ($Ca_2Al_2SiO_7$) and/or akermanite ($Ca_2MgSi_2O_7$), Calcium-magnesium aluminosilicates are among the common origins of the source S. These peaks testify to an unreacted retained S mineral or to secondary crystalline products resulting from anastomosis during the onset of hydration and curing. Notably, no peaks are observed near 18° or 29.4° 2θ, excluding the presence of portlandite ($Ca(OH)_2$) or calcite ($CaCO_3$), and hence testifying to an effective incorporation of released calcium into the amorphous gel, excluding precipitation as free lime and carbonates. This refers to an efficient immobilization and absorption of calcium cations from the S, boosting matrix stability and leaching resistance.

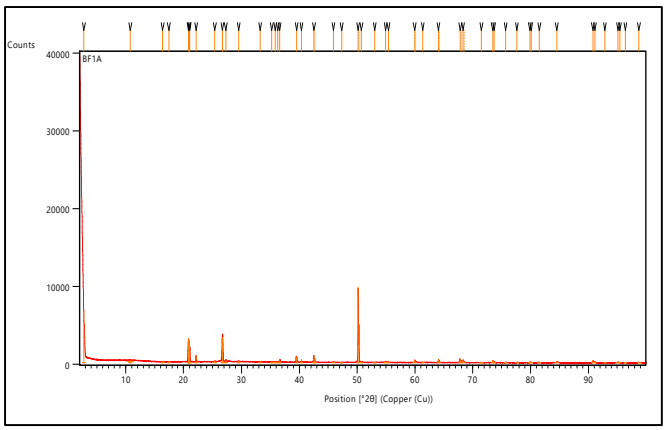

Fig. 8. XRD of GMs.

Overall intensity of the amorphous hump far overbalances the crystalline peaks, supporting the conclusion on the chemically prevailing and structurally continuous geopolymer network. This diffraction signature perfectly matches the previous SEM results, signifying a heterogeneously but essentially gel-linked matrix with dispersed unreacted FA and D residues. Therefore, the XRD supports the conclusion that the ternary reaction of the S, FA, and D precursors resulted in one polymerization-effective matrix, one where the majority of reactive moieties acted to produce amorphous gel, with only strongly constructed mineral entities (as mullite and quartz) remaining as crystalline residues. Regardless of whether exposed to ambient, thermally, or electrothermally curing, the general XRD imprint is the same due to the preservation of amorphous gel structure as the dominant phase and the minimal crystalline fraction, highlighting the structural imprint of successful geopolymerization within this complex blended system.

IV. CONCLUSIONS

- Ambient curing led to significantly lower mechanical strength, with only 28-day compressive strength and flexural strength of 20.59 MPa and 3.77 MPa, and the highest porosity (approximately 35%) and water absorption (approximately 20%). SEM analysis also affirmed an absent gel formation, extensive formation of capillary pores, and presence of unreacted spherical Fly Ash (FA) and angular diatomite (D) particles, leading to structurally weak and chemically immature matrices.
- Thermal curing with a higher temperature of 80°C developed the highest average 28-day compressive strength (35.03 MPa) and exceeded the strength of the ambient-curing counterpart by as much as 72.9%. This enhanced strength culminated from complete dissolution of precursors and an uniform C–A–S–H/N–A–S–H gel network as confirmed from SEM/EDS examinations, with no longer recognizable spherical FA and Slag (S) particles, and no occurrence of microcracks or ITZ discontinuities.
- Electrothermal Curing (EC) with 30 V exhibited a gradual but consistent strength gain behavior, reaching 27.65 MPa compressive strength at 24h (1.55× ambient strength) and 3.78 MPa flexural strength, with no retrogression. Although less efficient than 40 V, its flexural strength-compressive strength ratio (approximately 0.137) and energy efficiency (0.92 MPa/V in compressive strength) confirmed 30 V as an adequate low-voltage curing method for gradual strength increase under off-grid or budget-conscious situations. Overactivation with 50 V led to regression of both compressive strength and flexural strength values. Even with initially high energy input, the compressive strength at 24h dropped to 18.39MPa and flexural strength to 3.38MPa, proving the "activation ceiling" principle—high voltage led to microcracking, shrinkage-induced destabilization of pore structure, and structural discontinuity due to uncontrollable internal drying, evidenced with SEM as incomplete dissolution of precursors and fracturing of the gel phase.
- EC with 40 V outperformed all the other regimes on all mechanical, physical, and microstructural indicators, producing the best balance between build-up of strength and integrity of the microstructure. A curing time of 4 hours with 40 V resulted in reaching 88% of the thermal standard compressive strength, with 31.34 MPa, only 14% of the time, and had the most significant value of flexural strength (5.66 MPa), better than the thermal equivalent by 4%, and thus, establishing its unique capability towards fast precast or accelerated modular building applications.

- Physical performance ensured lower porosity and absorption below 40 V and 50 V curing, with porosity values lowered to approximately 10–12%, absorption to 4–6%, and bulk densities above 2.10 g/cm³. Pairwise scatter plots revealed strong negative correlations between bulk density and absorption/porosity, indicating that improved bulk density with electrical curing led to better durability characteristics. Ambient-curing samples clustered with the low bulk density (<2.00 g/cm³) and high capillarity. EC samples, especially 40 V, formed closely grouped, high-density clusters, reinforcing the method's repeat and scale ability.
- Multi-Criteria Decision Making (MCDM) and fuzzy logic analysis conclusively ranked 40 V curing as the top performer, followed closely by Weighted Sum Model (WSM), Weighted Product Model (WPM), and fuzzy with ratings of 0.857, 0.840, and 0.866, respectively. It consistently outperformed thermal (second rank of all the models) and markedly outperformed 30 V and 50 V, exhibiting inconsistent or penalized performances due to imbalanced strength and durability parameters trade-offs.
- SEM/EDS imaging unambiguously segregated curing regimes' effects: porous, inert particle bearing samples agreed with ambient ones; thermally set samples demonstrated complete gel continuity and particle dissolution; while 40 V electro-curing samples possessed heterogeneously but partially successful reaction fronts with localized gel bridges, softening of the precursors, and variable densification consistent with existing paths—showing uniform electrode design and flow control are required to scale the process.
- XRD analysis corroborated microstructural results, showing dominant amorphous humps between 22°–38° 2θ characteristic of N–A–S–H/C–A–S–H gels, indicating successful geopolymerization. Minor residual crystalline peaks from quartz (approximately 26.6°), mullite (approximately 27.9°), and gehlenite/akermanite (approximately 36.5°–59.9°) indicated limited unreacted phases from S and FA. Specifically, no peaks of $Ca(OH)_2$ or $CaCO_3$ appeared, confirming successful immobilization of Ca and absence of dangerous crystalline products.

DATA AVAILABILITY

The dataset generated during and/or analyzed during the current study can be available from the corresponding author upon reasonable request.

REFERENCES

[1] L. Y. Ming, O. W. En, H. C. Yong, M. M. A. B. Abdullah, and O. S. Ween, "Characteristic of One-Part Geopolymer as Building Materials," in *Sustainable Waste Utilization in Bricks, Concrete, and Cementitious Materials*, vol. 129, A. Abdul Kadir, N. Amira Sarani, and S. Shahidan, Eds., Singapore: Springer Singapore, 2021, pp. 97–118.

[2] T. Luukkonen, Z. Abdollahnejad, J. Yliniemi, P. Kinnunen, and M. Illikainen, "One-part Alkali-activated Materials: A review," *Cement and Concrete Research*, vol. 103, pp. 21–34, Jan. 2018, https://doi.org/10.1016/j.cemconres.2017.10.001.

[3] T. Mukhametkaliyev, Md. H. Ali, V. Kutugin, O. Savinova, and V. Vereschagin, "Influence of Mixing Order on the Synthesis of Geopolymer Concrete," *Polymers*, vol. 14, no. 21, Nov. 2022, Art. no. 4777, https://doi.org/10.3390/polym14214777.

[4] S. V. Vassilev, C. G. Vassileva, A. I. Karayigit, Y. Bulut, A. Alastuey, and X. Querol, " Phase–mineral and Chemical Composition of Composite Samples From Feed Coals, Bottom Ashes and Fly Ashes at the Soma Power Station, Turkey," *International Journal of Coal Geology*, vol. 61, no. 1–2, pp. 35–63, Jan. 2005, https://doi.org/10.1016/j.coal.2004.06.004.

[5] A. I. Karayigit, Y. Bulut, X. Querol, A. Alastuey, and S. Vassilev, "Variations in Fly Ash Composition from the Soma Power Plant, Turkey," *Energy Sources*, vol. 27, no. 15, pp. 1473–1481, Nov. 2005, https://doi.org/10.1080/009083190523811.

[6] A. Baba, G. Gurdal, and F. Sengunalp, " Leaching Characteristics of Fly Ash From Fluidized Bed Combustion Thermal Power Plant: Case Study: Çan (çanakkale-turkey)," *Fuel Processing Technology*, vol. 91, no. 9, pp. 1073–1080, Sept. 2010, https://doi.org/10.1016/j.fuproc.2010.03.015.

[7] S. Ural, " Comparison of Fly Ash Properties from Afsin-Elbistan Coal Basin, Turkey," *Journal of Hazardous Materials*, vol. 119, no. 1–3, pp. 85–92, Mar. 2005, https://doi.org/10.1016/j.jhazmat.2004.10.024.

[8] İ. Alp, H. Deveci, and H. Süngün, " Utilization of Flotation Wastes of Copper Slag as Raw Material in Cement Production," *Journal of Hazardous Materials*, vol. 159, no. 2–3, pp. 390–395, Nov. 2008, https://doi.org/10.1016/j.jhazmat.2008.02.056.

[9] I. Yuksel, O. Ozkan, and T. Bilir, "Use of Granulated Blast-Furnace Slag in Concrete as Fine Aggregate," *ACI Materials Journal*, vol. 103, no. 3, 203–208, 2006, https://doi.org/10.14359/15854.

[10] E. Özbay, M. Erdemir, and H. İ. Durmuş, " Utilization and Efficiency of Ground Granulated Blast Furnace Slag on Concrete Properties – A Review," *Construction and Building Materials*, vol. 105, pp. 423–434, Feb. 2016, https://doi.org/10.1016/j.conbuildmat.2015.12.153.

[11] G. Tozsin, F. Yonar, O. Yucel, and A. Dikbas, "Utilization Possibilities of Steel Slag as Backfill Material in Coastal Structures," *Scientific Reports*, vol. 13, no. 1, Mar. 2023, Art. no. 4318, https://doi.org/10.1038/s41598-023-31156-z.

[12] M. Ozturk and G. Arslan, "Shear Behavior of Granulated Blast Furnace Slag-Based Geopolymer-Reinforced Concrete Beams," *Buildings*, vol. 12, no. 12, Nov. 2022, Art. no. 2053, https://doi.org/10.3390/buildings12122053.

[13] F. A. Turkey, S. Bt. Beddu, A. N. Ahmed, and S. K. Al-Hubboubi, " Effect of High Temperatures on the Properties of Lightweight Geopolymer Concrete Based Fly Ash and Glass Powder Mixtures," *Case Studies in Construction Materials*, vol. 17, Dec. 2022, Art. no. e01489, https://doi.org/10.1016/j.cscm.2022.e01489.

[14] Y. Lv, C. Wang, W. Han, X. Li, and H. Peng, "Study of the Mechanical Properties and Microstructure of Alkali-Activated Fly Ash–Slag Composite Cementitious Materials," *Polymers*, vol. 15, no. 8, Apr. 2023, Art. no. 1903, https://doi.org/10.3390/polym15081903.

[15] K. Şahbudak, "Mechanical and Thermal Evaluation of Diatomite Doped Fly Ash Based Geopolymers," *Materials Science*, vol. 28, no. 1, pp. 75–81, Feb. 2022, https://doi.org/10.5755/j02.ms.26796.

[16] C. Bagci, G. P. Kutyla, and W. M. Kriven, " Fully Reacted High Strength Geopolymer Made With Diatomite as a Fumed Silica Alternative," *Ceramics International*, vol. 43, no. 17, pp. 14784–14790, Dec. 2017, https://doi.org/10.1016/j.ceramint.2017.07.222.

[17] H. Mohamedbakr and M. Burkitbaev, "Elaboration and Characterization of Natural Diatomite in Aktyubinsk/Kazakhstan," *The Open Mineralogy Journal*, vol. 3, no. 1, pp. 12–16, June 2009, https://doi.org/10.2174/1874456700903010012.

[18] K. Pławecka, A. Bąk, M. Hebdowska-Krupa, and M. Łach, "The Use of Calcined Diatomite as an Additive to Geopolymeric Materials," in *10th MATBUD'2023 Scientific-Technical Conference*, Feb. 2023, Art. no. 28, https://doi.org/10.3390/materproc2023013028.

[19] A. Noushini and A. Castel, " The Effect of Heat-curing on Transport Properties of Low-calcium Fly Ash-based Geopolymer Concrete," *Construction and Building Materials*, vol. 112, pp. 464–477, June 2016, https://doi.org/10.1016/j.conbuildmat.2016.02.210.

[20] H. Ürünveren, A. Beycioğlu, E. Ç. Resuloğulları, and N. B. Dişken, " A Comparative Investigation of Eco-friendly Fly Ash-based Geopolymer

Mortar Produced by Using Electrical and Heat Curing: Mechanical Properties, Energy Consumption and Cost," *Construction and Building Materials*, vol. 439, Aug. 2024, Art. no. 137200, https://doi.org/10.1016/j.conbuildmat.2024.137200.

[21] S. Ilkentapar *et al.*, " Evaluation of Diatomite Substitute With Thermal Power Plant Waste Fly Ash in Sustainable Geopolymer Through Life Cycle Assessment," *Journal of Material Cycles and Waste Management*, vol. 27, no. 3, pp. 1418–1435, May 2025, https://doi.org/10.1007/s10163-025-02184-w.

[22] S. Ilkentapar and E. Orklemez, "Uçucu Kül Esaslı Geopolimer Harçlara Diatomit İkamesinin Isı İletkenliğe Etkisi," *Erciyes Üniversitesi Fen Bilimleri Enstitüsü Dergisi*, vol. 36, no. 3, pp. 312–324, Dec. 2020.

[23] X. Ge, X. Hu, H. Li, and C. Shi, "Synergistic Effect of Characteristics of Raw Materials on Controlling the Mechanical Properties of Fly Ash-based Geopolymers," *Cement and Concrete Composites*, vol. 145, Jan. 2024, Art. no. 105368, https://doi.org/10.1016/j.cemconcomp.2023.105368.

[24] X. Guan, W. Luo, S. Liu, A. G. Hernandez, H. Do, and B. Li, " Ultra-high Early Strength Fly Ash-based Geopolymer Paste Cured by Microwave Radiation," *Developments in the Built Environment*, vol. 14, Apr. 2023, Art. no. 100139, https://doi.org/10.1016/j.dibe.2023.100139.

[25] M. Nykiel *et al.*, "The Influence of Diatomite Addition on the Properties of Geopolymers Based on Fly Ash and Metakaolin," *Materials*, vol. 17, no. 10, May 2024, Art. no. 2399, https://doi.org/10.3390/ma17102399.

[26] T. Nongnuang, P. Jitsangiam, U. Rattanasak, and P. Chindaprasirt, " Novel Electromagnetic Induction Heat Curing Process of Fly Ash Geopolymer Using Waste Iron Powder as a Conductive Material," *Scientific Reports*, vol. 12, no. 1, June 2022, Art. no. 9530, https://doi.org/10.1038/s41598-022-13392-x.

[27] Y. Zhang *et al.*, " Electrothermal Effect of Alternating Current on Hardening Process of Metakaolin-based Geopolymer," *Cement and Concrete Composites*, vol. 142, Sept. 2023, Art. no. 105205, https://doi.org/10.1016/j.cemconcomp.2023.105205.

[28] S. Vaidya, E. I. Diaz, and E. N. Allouche, "Experimental Evaluation of Self-Cure Geopolymer Concrete for Mass Pour Applications," in *World of Coal Ash Conference*, Denver,CO,USA, May 2011.

[29] S. Abubakri, P. S. Mangat, V. Starinieri, and G. R. Lomboy, " Electric Curing Parameters of Mortar and Its Mechanical Properties in Cold Weather," *Construction and Building Materials*, vol. 314, Jan. 2022, Art. no. 125615, https://doi.org/10.1016/j.conbuildmat.2021.125615.

[30] J. Cai, X. Li, J. Tan, and B. Vandevyvere, " Fly Ash-based Geopolymer with Self-heating Capacity for Accelerated Curing," *Journal of Cleaner Production*, vol. 261, July 2020, Art. no. 121119, https://doi.org/10.1016/j.jclepro.2020.121119.

[31] Z. Yang *et al.*, "A Comparative Study on the Mechanical Properties and Microstructure of Cement-Based Materials by Direct Electric Curing and Steam Curing," *Materials*, vol. 14, no. 23, Dec. 2021, Art. no. 7407, https://doi.org/10.3390/ma14237407.

[32] A. Yvette Sunga, S. Abubakri, G. Lomboy, I. Mantawy, D. Kennedy, and B. Watts, "Electric Curing of Conductive Concrete for Cold Weather," presented at the IABSE Symposium, Manchester 2024: Construction's Role for a World in Emergency, Manchester, United Kingdom, 2024, pp. 789–797, https://doi.org/10.2749/manchester.2024.0789.

[33] M. I. Batyuk, A. I. Gnyrya, V. Y. Ushakov, and S. V. Korobkov, " Rapid Direct Electric Heating of Fresh Concrete," *Journal of Physics: Conference Series*, vol. 1989, no. 1, Aug. 2021, Art. no. 012024, https://doi.org/10.1088/1742-6596/1989/1/012024.

[34] T. Uygunoğlu and İ. Hocaoğlu, " Effect of Electrical Curing Application on Setting Time of Concrete With Different Stress Intensity," *Construction and Building Materials*, vol. 162, pp. 298–305, Feb. 2018, https://doi.org/10.1016/j.conbuildmat.2017.12.036.

[35] M. S. Amouri and N. M. Fawzi, "The Mechanical Properties of Fly Ash and Slag Geopolymer Mortar with Micro Steel Fibers," *Engineering, Technology & Applied Science Research*, vol. 12, no. 2, pp. 8463–8466, Apr. 2022, https://doi.org/10.48084/etasr.4855.

[36] A. Nazari and G. Khalaj, " Prediction Total Specific Pore Volume of Geopolymers Produced From Waste Ashes by Fuzzy Logic," *Materials Research*, vol. 15, no. 2, pp. 242–252, Feb. 2012, https://doi.org/10.1590/S1516-14392012005000010.

[37] F. Özcan, C. D. Atiş, O. Karahan, E. Uncuoğlu, and H. Tanyildizi, " Comparison of Artificial Neural Network and Fuzzy Logic Models for Prediction of Long-term Compressive Strength of Silica Fume Concrete," *Advances in Engineering Software*, vol. 40, no. 9, pp. 856–863, Sept. 2009, https://doi.org/10.1016/j.advengsoft.2009.01.005.

[38] A. Nazari, " Application of Fuzzy Logic for Prediction Compressive Strength of Opc Based Geopolymers," *Materials Technology*, vol. 27, no. 5, pp. 364–370, Nov. 2012, https://doi.org/10.1179/1753555712Y.0000000021.

[39] I. Emovon and O. S. Oghenenyerovwho, " Application of MCDM Method in Material Selection for Optimal Design: A Review," *Results in Materials*, vol. 7, Sept. 2020, Art. no. 100115, https://doi.org/10.1016/j.rinma.2020.100115.